RESEARCH ARTICLE

NANO · MICRO small
www.small-journal.com

An Alloy Nanowire-Based Water Splitting Electrode Adapting Fluctuating Electric Power Input

*Yunyi Jia, Hongjie Liu, Jingjing Weng, Lumeng Wang, Ju Chen, Rui Yao, Yunxiang Zhao, Weisheng Pan, Shunhang Hua, Caiwu Liang, Johnny C. Ho, and Cheng Yang**

Water electrolysis is a promising strategy for storing surplus renewable electricity in the form of green hydrogen. However, the intermittent nature of renewable power causes frequent start-stop cycles in electrolyzers, inducing reverse current, which accelerates catalyst degradation and compromises electrode durability. Despite its long-standing industrial relevance, the understanding of irreversible damage mechanisms under dynamic cycling and effective mitigation remains limited. Here, a self-supported ternary alloy nanowire electrode is presented with exceptional tolerance to intermittent operation via synergistic structural and electronic regulation. The assembled anion membrane electrolyzer delivers a low cell voltage of 2.33 V at 4 A cm^{-2} and maintains stable performance over 900 h at 1 A cm^{-2}. Under 2000 cycles of intermittent reverse current, the ternary alloy electrode exhibits ≈40% lower voltage decay than its binary NiFe counterpart. The nanowire architecture, combining high surface area and mechanical flexibility, facilitates efficient gas bubble release and alleviates local stress. Incorporation of cobalt stabilizes active sites by increasing vacancy formation energy and tuning the electronic structure, thereby mitigating degradation caused by reverse current pulses. This work establishes a benchmark for reverse-current adaptive electrode design for water splitting, promoting stable hydrogen production and storage under intermittent renewable energy sources.

1. Introduction

Hydrogen has emerged as a key energy carrier in the transition toward a sustainable and carbon-neutral energy future.[1–3] Integrating renewable energy with water electrolysis enables the storage and utilization of hydrogen, facilitating grid load balancing and enhancing the efficiency and flexibility of renewable energy systems.[4,5] This approach provides a promising route to convert intermittent electricity into storable chemical energy, thereby enabling large-scale deployment of green hydrogen technologies.

Under practical deployment scenarios, renewable electricity is prioritized for direct grid supply, particularly during peak demand periods, while surplus low-cost off-grid power is allocated to hydrogen production (**Figure 1a**).[6] However, the inherently intermittent and fluctuating nature of surplus renewable electricity poses significant challenges to the stability and long-term reliability of water electrolysis systems. To utilize such power efficiently, electrolyzers inevitably undergo frequent start–stop cycles, which induce spontaneous electrochemical responses such as reverse current (Figure 1b).[7] In practical alkaline water electrolyzers, particularly in parallel-stack configurations prone to current redistribution, reverse currents are commonly observed during sudden shutdowns or voltage drops.[8] Electrochemical measurements confirm this phenomenon: when the cell voltage in a Pt/C || IrO_2 electrolyzer abruptly drops from 2 to 0 V,

Y. Jia, H. Liu, J. Weng, L. Wang, J. Chen, R. Yao, Y. Zhao, W. Pan, S. Hua, C. Yang
Institute of Materials Research
Tsinghua Shenzhen International Graduate School
Tsinghua University
Shenzhen 518055, China
E-mail: yang.cheng@sz.tsinghua.edu.cn

C. Liang
Department of Materials
Imperial College London
London 4615, UK

C. Liang
Department of Chemistry
Centre for Processable Electronics
Imperial College London
London 4615, UK

J. C. Ho
Department of Materials Science and Engineering
City University of Hong Kong
Hong Kong SAR 53025, China

J. C. Ho
State Key Laboratory of Terahertz and Millimeter Waves
City University of Hong Kong
Hong Kong SAR 53025, China

J. C. Ho
Institute for Materials Chemistry and Engineering
Kyushu University
Fukuoka 8190382, Japan

The ORCID identification number(s) for the author(s) of this article can be found under https://doi.org/10.1002/smll.202509828

DOI: 10.1002/smll.202509828

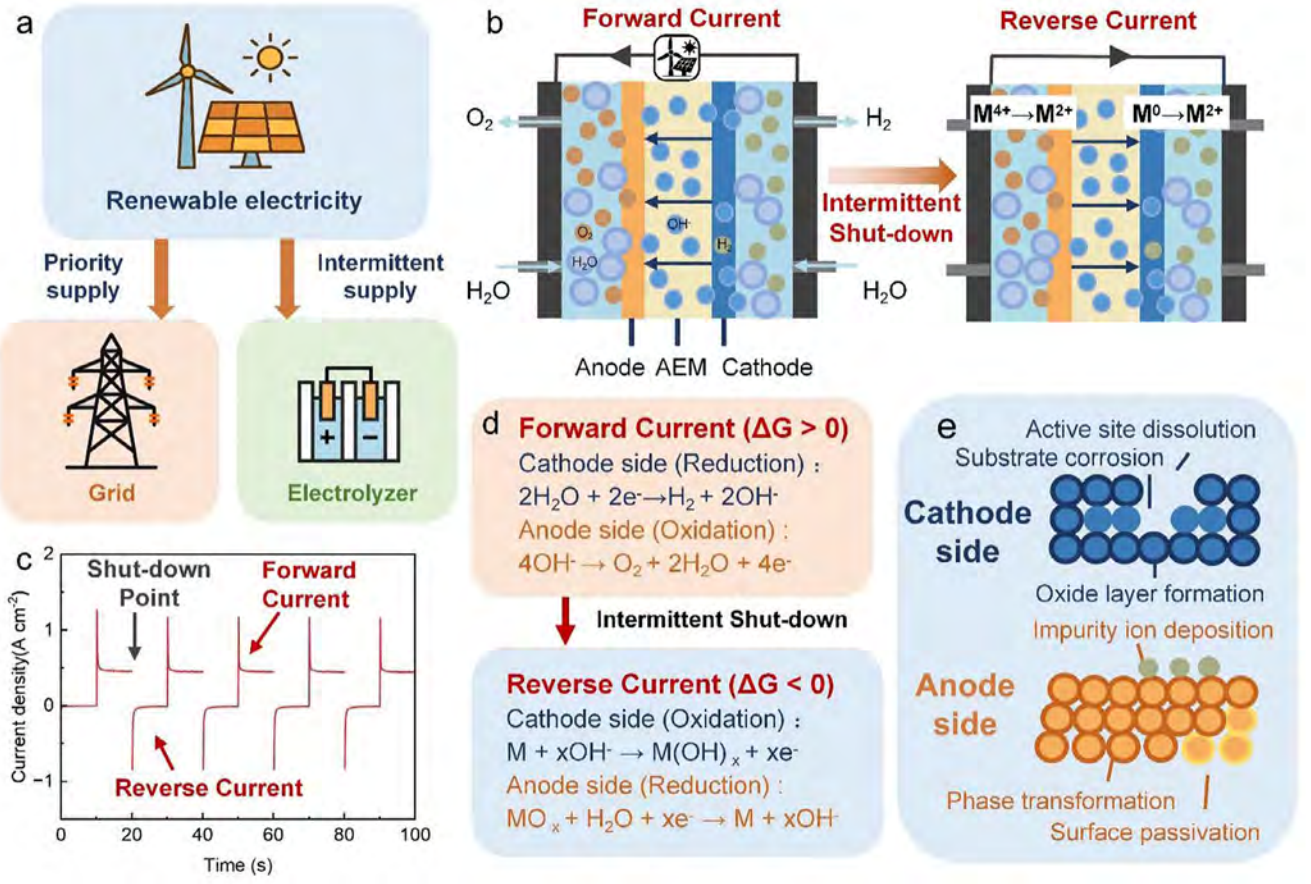

Figure 1. Reverse current phenomenon in renewable energy-driven water electrolysis systems. a) Renewable electricity is prioritized for grid supply; excess energy can be directed to water electrolysis for hydrogen production. b) Reverse current phenomenon in electrolyzer systems. c) The reverse current phenomenon occurs when the voltage is switched between 0 and 2 V. d) Electrochemical reactions during the self-driven reverse current process. e) Proposed mechanism for reverse-current-induced electrode degradation.

a reverse current density exceeding 1 A cm^{-2} appears during the transient decay phase (Figure 1c). The reverse current originates primarily from a sharp potential gradient formed between oxidized species at the anode and accumulated reductive intermediates at the cathode during sudden shutdown or voltage drop (Figure 1d).[9] This gradient induces a directional electric field across electron-conducting bipolar plates, while ion migration along the ion-exchange membrane establishes a dual-channel charge transport pathway comprising both electronic and ionic conduction. This self-driven charge transport process, powered by internal chemical potential, results in a reverse current from the cathode to the anode.

Reverse current is not merely a superficial phenomenon but can cause detrimental effects on electrode materials, including metal dissolution, electrode deactivation, and structural damage (Figure 1e).[10,11] At the cathode side, it drives surface oxidation, forming insulating oxides that block active sites and compromise stability.[12] In transition metal catalysts, high-valent species dissolve irreversibly under high potential, disrupting the catalytic layer and accelerating aging.[13] Moreover, positive potentials also degrade conductive supports, leading to catalyst detachment and increased resistance.[14] Recent studies further reveal that reverse current can trigger Ni/Fe dissolution, lattice reconstruction, and local pH fluctuations, which synergistically destabilize the catalyst framework and induce irreversible phase transitions.[15] Similar polarity-reversal-induced corrosion has been reported for RuO_2 electrodes, where hydroxylated phases dissolve into soluble ruthenates, further highlighting the susceptibility of transition-metal oxides to such electrochemical stress.[16] At the anode, reverse currents induce reductive transformations that modify surface chemistry, forming low-activity oxides or depositing reduced impurities, diminishing oxygen evolution efficiency. For Ni-based catalysts, it reduces active NiOOH back to $Ni(OH)_2$ or inert phases, causing passivation. Additionally, impurity deposition, phase transitions, and mechanical stress contribute to particle fracture and delamination, further accelerating degradation.[17]

Exploring catalyst systems that resist fluctuating current inputs, along with understanding stability enhancement mechanisms, is vital for optimizing the compatibility of electrolyzers with renewable energy under various operational conditions. NiFe-based catalysts are archetypes of high-performance electrocatalysts for water splitting under alkaline conditions. Their widespread application underscores the necessity to probe how these catalysts respond to variable energy inputs. However, these catalysts face stability challenges, particularly rapid degradation

during prolonged reactions, primarily due to the loss of active sites from ion segregation and structural degradation.[18,19]

Recent studies have shown that incorporating guest elements into catalyst alloys can enhance structural stability, particularly by mitigating metal dissolution during catalytic processes.[20] Meanwhile, introducing additional elements to the electrode can promote hydrogen evolution reaction (HER) performance, and thus these bifunctional electrodes have emerged as a potential solution, capable of meeting the demands of both anodic and cathodic applications simultaneously. However, previous studies have predominantly focused on the catalytic activity in static testing conditions, while these testing protocols often diverge significantly from practical operating environments. Under practical intermittent inputs, alloy electrodes may experience rapid degradation due to frequent potential fluctuations and current reversals. These conditions can induce redox transitions, local pH shifts, and gas bubble accumulation, leading to phase instability and structural damage, hindering the adoption of high-performance multimetallic or nanostructured catalysts in commercial alkaline water electrolysis (AWE) and anion exchange membrane water electrolysis (AEMWE) systems. Yet, direct evidence demonstrating improved resistance to reverse current induced degradation, which presents a major challenge for electrolyzer operation under intermittent renewable power, is still lacking. Research on this degradation mechanism is remains limited, and comprehensive benchmark studies for its mitigation have yet to be conducted.

In this work, we benchmark the performance of cobalt-incorporated NiFe-based electrodes under intermittently reversed current conditions and provide the first experimental evidence that cobalt incorporation significantly enhances resistance to reverse current-induced degradation. Specifically, we have developed a $Ni_{75}Fe_{15}Co_{10}$ (at.%) nanowire electrode (NFCW) with enhanced structural stability, which exhibits superior service life under fluctuating power inputs compared to binary nickel–iron alloys. The introduction of cobalt stabilizes the NiFe coordination environment by increasing vacancy formation energy, effectively mitigating metal dissolution under harsh conditions. NFCW demonstrates exceptional bifunctional performance for both the hydrogen evolution reaction (HER) and oxygen evolution reaction (OER). When assembled in an AEMWE cell, the NFCW electrode demonstrates high operational efficiency and stability, requiring only 2.33 V to deliver 4 A cm^{-2} and maintains stable operation at 1 A cm^{-2} for over 900 h. After 2000 cycles of intermittent reverse current, it reduces the voltage decay rate by ≈40% compared to a binary NiFe electrode, demonstrating remarkable resilience to dynamic current fluctuations. These results support its potential for integration into systems powered by intermittent renewable energy sources.

2. Results and Discussion

2.1. Synthesis and Structural Characterization

The alloy nanowire electrodes were synthesized via a magnetic field-assisted chemical reduction method (**Figure 2a**). By precisely controlling the reduction of Ni^{2+}, Fe^{2+}, and Co^{2+} ions under a directional magnetic field, vertically aligned nanowires with an interconnected 3D network were obtained (Figure S1, Supporting Information). The precursor ratios of nickel, iron, and cobalt are detailed in Table S1 (Supporting Information), with ICP-OES analysis confirming the compositions (Table S2, Supporting Information). Among the synthesized compositions, the optimal $Ni_{75}Fe_{15}Co_{10}$ exhibited superior electrocatalytic activity and is referred to as NFCW in this study (See Experiment Section in Supporting Information for details). NFCW demonstrates a diameter distribution ranging from 80 to 160 nm (Figure S2, Supporting Information). The initial bulk of the nanowires is fully mechanically compressible, and the resulting films can endure repeated bending tests (Figures S3 and S4, Supporting Information), which is important for mechanical stress dissipation and protection of the catalyst structure against bubble-induced impact and delamination. Using the same synthetic method, we produced nanowire-integrated electrodes with varying compositions, including Nickel Nano-Wires electrodes (NW) and Nickel-Iron Alloy Nano-Wires electrodes (NFW) (Figures S5 and S6, Supporting Information). NFCW can be easily reshaped into self-supported film electrodes of various sizes through mechanical pressing (Figure S7, Supporting Information), owing to its lamellar porous structure (Figure S8, Supporting Information), which adapts to stress and withstands rapid bubble impact. This structure exhibits a high Brunauer–Emmett–Teller (BET) specific surface area of 7.58 m^2 g^{-1} (Figure S9, Supporting Information), facilitating easy access of reactants to the catalytic sites. Additionally, contact angle measurements reveal the superior hydrophilicity of NFCW (Figure S10, Supporting Information).

High-resolution structural analyses reveal the hierarchical architecture of NFCW. Transmission electron microscopy (TEM) reveals the uniform alignment of nanowires, while selected-area electron diffraction (SAED) patterns (Figure 2c) exhibit four distinct rings indexed to the (111), (200), (220), and (311) planes of a face-centered cubic (FCC) lattice. High-resolution TEM (HRTEM) further uncovers a well-defined core–shell structure (Figure 2d). The ordered crystalline core exhibits an interplanar spacing of 0.206 nm (matching the FCC (111) plane) (Figure S11, Supporting Information), while the surface transitions to an amorphous oxide layer. The amorphous area observed on the surface indicates the presence of oxidation state species, likely due to oxidation and hydroxide formation during and after synthesis. This amorphous oxide layer can function as a protective shell, mitigating surface reconstruction under electrochemical conditions and thereby reducing the direct exposure and dissolution of underlying metal atoms. Energy-dispersive X-ray spectroscopy (EDX) mapping shows that Ni, Fe, and Co are uniformly distributed across the nanowires (Figure 2e). X-ray diffraction (XRD) analysis in Figure 2f reveals intense peaks at ≈44.5°, 51.6°, and 76.0° for NCFW. The absence of additional peaks suggests that Co incorporation does not disrupt the crystal lattice. Moreover, peak shifts to lower angles upon Fe and Co doping indicate lattice expansion and solid solution formation.[21] Increasing Co content results in reduced peak intensities, reflecting diminished crystallinity (Figure S12, Supporting Information).

X-ray photoelectron spectroscopy (XPS) further supports these findings, with the survey spectrum (Figure S13, Supporting Information) confirming the presence of Ni, Co, Fe, and O. Depth-resolved XPS spectra reveal that the majority of the nanowires remain in a metallic state, with only mild surface oxidation (Figure S14, Supporting Information). The O 1s spectrum

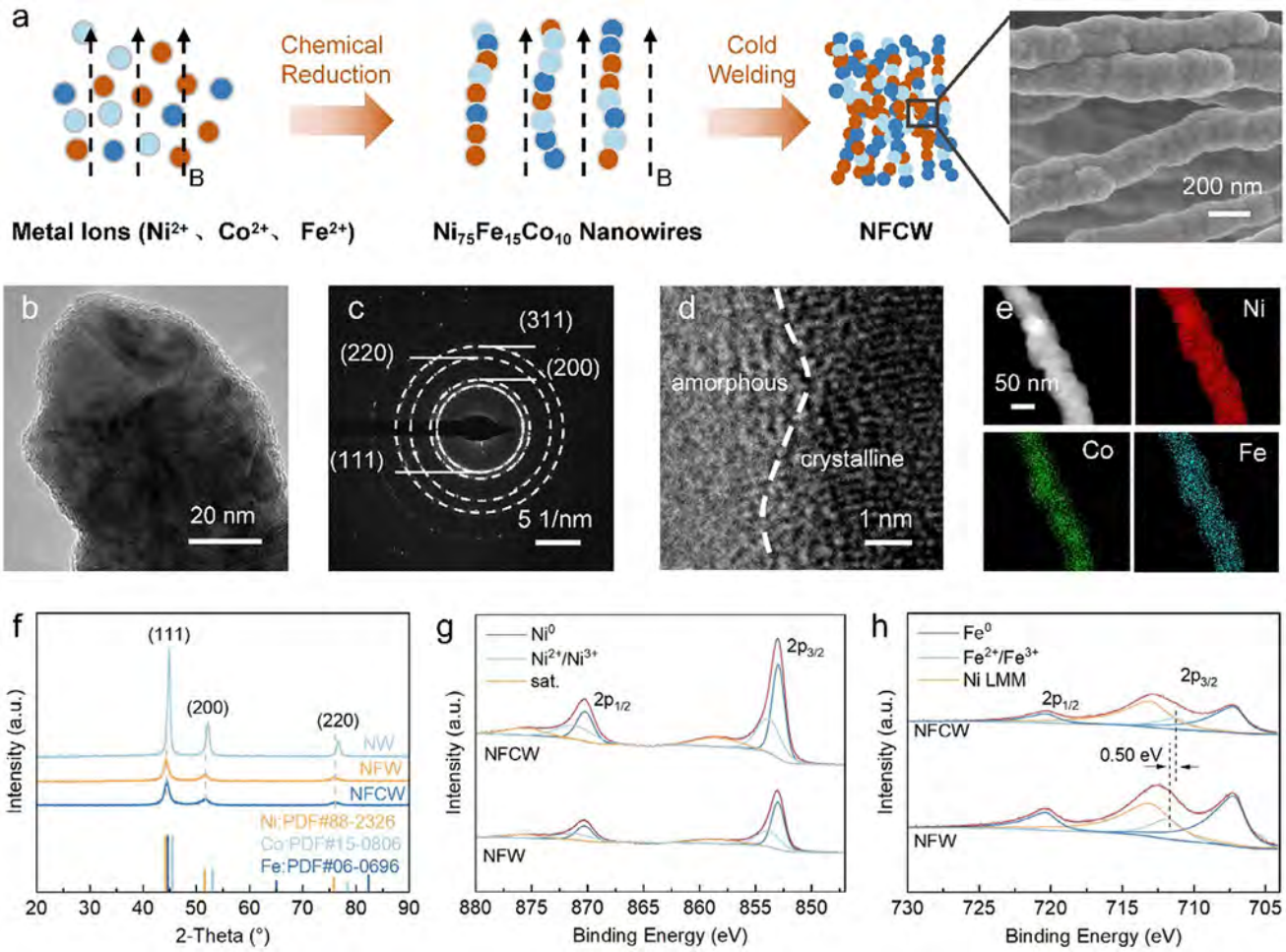

Figure 2. Synthesis and structural analysis of the NFCW. a) Schematic of the magnetic field-assisted preparation process and SEM image of NFCW. b) TEM image of NFCW. c) SAED pattern of NFCW. d) HRTEM image of NFCW. e) EDX elemental mapping. f) XRD patterns of NW, NFW, and NFCW. g) Ni 2p and h) Fe 2p XPS spectra of NFW and NFCW.

reveals three components: lattice oxygen (M-O) at ≈529.9 eV, mixed oxides/hydroxides (M-OH) at 531.3 eV, and water adsorption at 533.2 eV (Figure S14d, Supporting Information).[22] The Ni $2p_{3/2}$ signal can be deconvoluted into two main peaks at 852.8 and 853.9 eV, corresponding to Ni^0 and Ni^{2+}/Ni^{3+} (Figure 2g).[23] Fe 2p peaks at 707.24, 711.27, and 713.10 eV correspond to Fe^0, Fe^{2+}/Fe^{3+}, and Ni LMM (Figure 2h),[24,25] exhibiting a 0.50 eV shift toward the lower energy state. The Co $2p_{1/2}$ peaks at 778.4 and 779.8 eV correspond to Co^0 and Co^{2+}/Co^{3+} (Figure S15, Supporting Information).[26] The observed 0.50 eV low-energy shift in Fe 2p peaks suggest strong electronic interactions between Co and Ni/Fe, which stabilize the metallic phase by reducing surface defect density and oxidation propensity.[27]

2.2. Bifunctional Catalyst Performance and Kinetic Analysis

The HER/OER activities of different samples were evaluated in 1 M KOH using a standard three-electrode system. The results (Figures S16 and S17, Supporting Information) indicate that catalytic performance improves with increasing cobalt atomic ratios up to ≈10%, with minimal enhancement beyond this level. As illustrated in **Figure 3**a, NFCW exhibits excellent bifunctional catalytic performance, with HER overpotential of only 40 mV and OER overpotential of 220 mV at 10 mA cm^{-2}, outperforming both NW and NFW. NFCW demonstrates excellent catalytic efficiency, with Tafel slopes of 44 mV dec^{-1} for HER and 35 mV dec^{-1} for OER (Figure 3b) and low charge transfer resistances of 2.45 Ω for HER and 0.45 Ω for OER (Figure 3c), indicating rapid electron transfer and superior catalytic activity. The electrochemical surface area (ECSA) was further assessed, revealing a high double-layer capacitance (C_{dl}) of 76.55 mF cm^{-2} for NFCW, indicative of a large ECSA and abundant active sites (Figures S18 and S19, Supporting Information). To decouple intrinsic activity from geometric contributions, we further compared ECSA-normalized HER and OER activities (Figure S20, Supporting Information), which confirm that NFCW possesses superior intrinsic catalytic activity relative to NW and NFW. The OER and HER performance of NiFeCo powder still outperforms those of NiFe powder (Figure S21, Supporting Information), indicating that the powder catalyst also exhibits similar optimization effects. Furthermore, NFCW outperforms reported non-noble metal electrocatalysts in HER

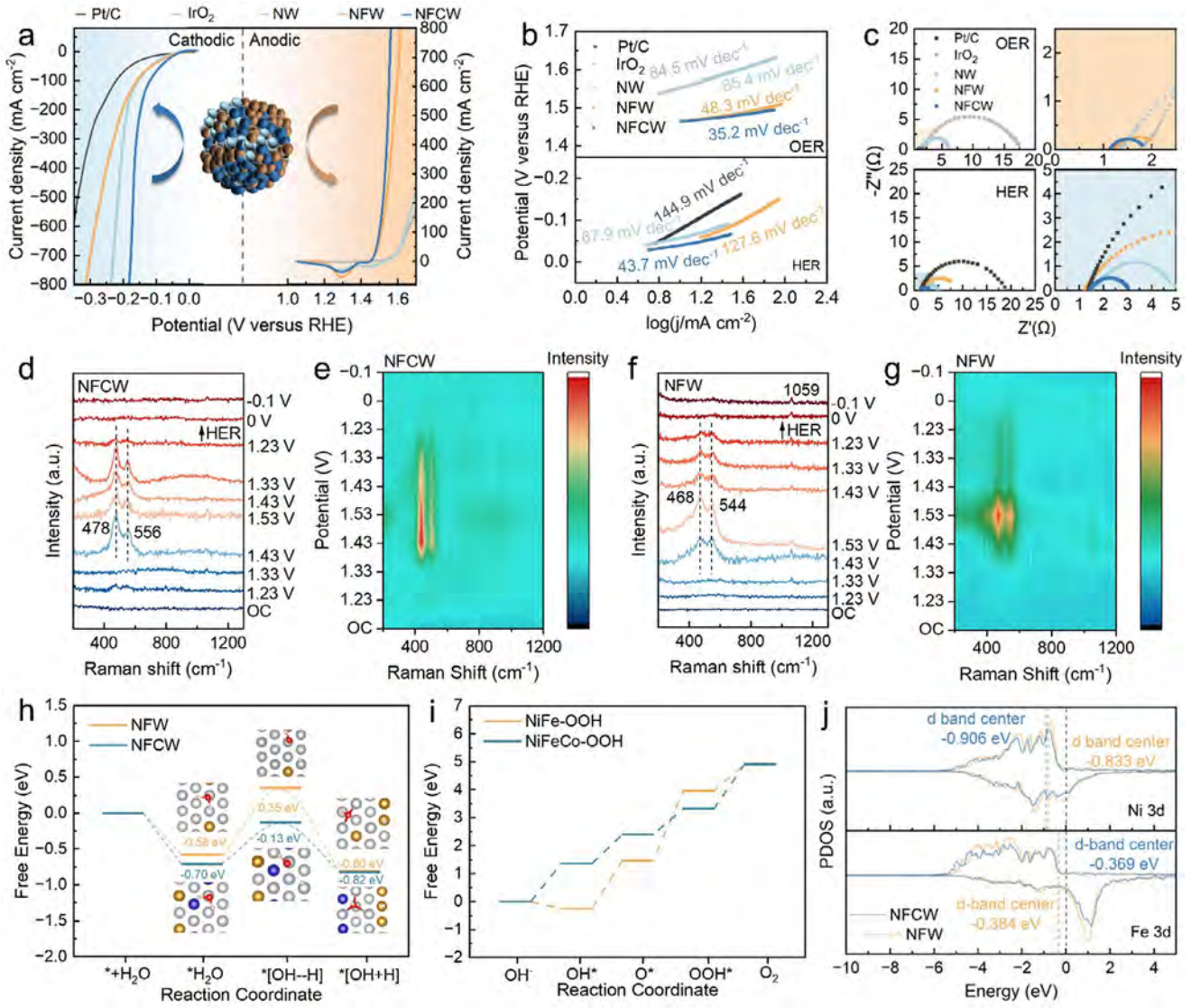

Figure 3. Electrochemical performance and DFT calculations of the NFCW. a) LSV curves of NFCW, NFW, NW, Pt/C, and IrO_2. The iR compensation values are listed in Table S3 (Supporting Information). b) Tafel plots. c) EIS Nyquist plots. d) In situ Raman spectra and e) the corresponding contour plot of NCFW. f) In situ Raman spectra and g) the corresponding contour plot of NFW. h) Gibbs free energy diagram of H2O dissociation in NFW and NFCW. Ni, Fe, Co, O, and H are represented by white, orange, and blue respectively. i) Gibbs free energy diagram for the four steps of the OER process in NiFeCo-OOH and NiFe-OOH. j) Projected density of states (PDOS) curves of Ni 3d and Fe 3d orbital.

and OER performance (Tables S4 and S5, Supporting Information).

In situ Raman spectroscopy was employed to probe the dynamic structural evolution and chemical bonding states of electrocatalysts. As shown in Figure 2d, two characteristic peaks emerge at 478 and 556 cm^{-1} with increasing applied potential. These are assigned to the depolarized E_g mode and the polarized A_{1g} stretch vibration of Ni-O in Fe, Co-doped γ-NiOOH.[28] The absence of Fe- or Co- specific oxide peaks in both ex situ and operando measurements confirms the successful lattice incorporation of heterometals rather than forming segregated oxide phases. Reversing the potential leads to a near-complete disappearance of these Raman features. The intensity ratio (I_{556}/I_{478}) serves as a quantitative descriptor of structural disorder, where lower values correlate with higher lattice distortion.[29,30] The ratios for NW, NFW, and NFCW are 1.82, 1.31, and 1.20, respectively, suggesting an increase in structural disorder, likely due to the incorporation of Fe and Co into the NiOOH lattice. During the OER process, the surface primarily exists in the form of Ni(FeCo)-LDH. Upon reaching the OER potential, it in situ transforms into Ni(FeCo)OOH, which serves as the active phase. Conversely, during HER, the surface reverts to a metallic state, where the pure metal phase acts as the active site.

To elucidate the origin of the electrocatalytic performance from an electronic structure perspective, density functional theory (DFT) calculations were conducted. As shown in Figure 3h, NFCW exhibits a lower ΔG for the water dissociation step ($*H_2O \rightarrow *[OH—H] \rightarrow [OH + H]$), indicating easier water

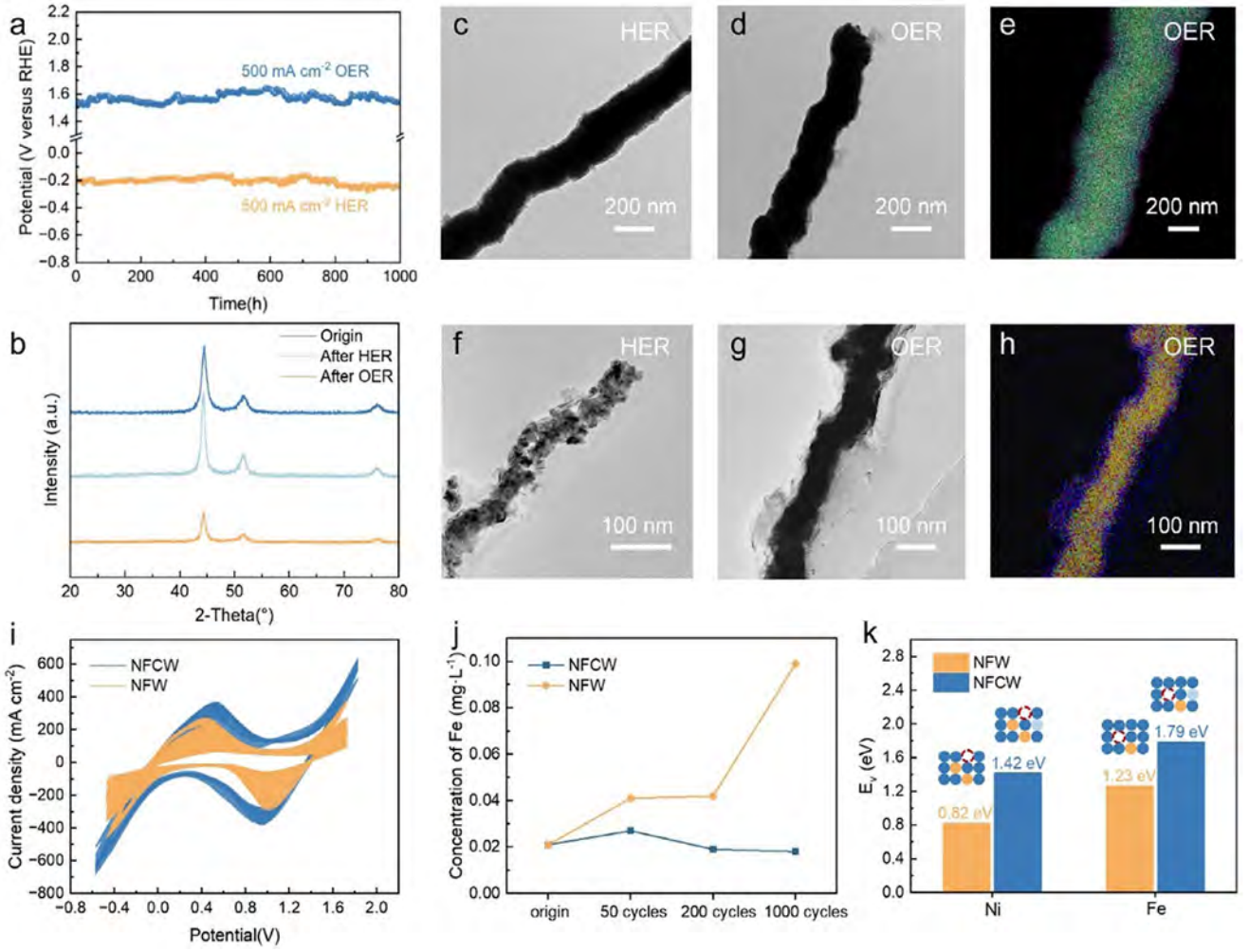

Figure 4. Stability evaluation. a) Stability test of NFCW at ± 500 mA cm^{-2} in 1 M KOH. The data fluctuations are due to electrolyte replacement and bubble evolution. b) XRD pattern of NFCW after low-term HER/OER. c,d) TEM images of NFCW after 1000 h of HER and OER. e) EDX elemental mapping of NFCW post-OER; purple denotes oxygen f,g) TEM images of NFW after 500 h of HER and OER. h) EDX elemental mapping of NFW post-OER; purple denotes oxygen. i) CV cycling Accelerated durability test (CV-ADT). j) ICP-OES analysis of Fe ion concentration in electrolytes after CV-ADT. k) Calculated vacancy formation energy for Ni/Fe sites.

dissociation and an accelerated HER process. NFCW also demonstrates a markedly reduced ΔG_{*H}, reflecting accelerated adsorption/desorption processes and enhanced HER activity (Figure S24, Supporting Information), and the models for the OER process are presented (Figures S25 and S26, Supporting Information). DFT calculations reveal that the rate-determining step (RDS) for OER in NiFeCo-OOH is the transition from OOH* to O_2, which is different from O* → OOH* for NiFe-OOH. Notably, NiFeCo-OOH exhibits a lower Gibbs free energy for the RDS (Figure 3i). The improved process of NiFeCo-OOH from O* → OOH* confirms that Co doping can accelerate the formation of highly active NiFeCo-OOH species during OER, suggesting improved bond activation. The details of Gibbs free energy are given in Tables S6–S8 (Supporting Information). The projected density of states (PDOS) in Figure 3j shows that NFCW has a deeper d-band center of −0.906 eV for Ni 3d compared to NFW (−0.833 eV), demonstrating the promoted electron redistribution and weakened Ni-H interaction,[31] which is beneficial for hydrogen desorption. Meanwhile, the d-band center of Fe 3d shifts toward the Fermi level, which is beneficial to enhance the adsorption ability of oxygen-containing intermediates during the OER process, thereby reducing metal dissolution under high oxidation potentials.[32] Thus, Co doping is thought to stabilize the local coordination environment of Ni and Fe, reducing their dissolution and consequently enhancing the stability of the NFCW electrode.

2.3. Mechanism of Stability Enhancement

NFCW demonstrated exceptional long-term stability, exhibiting negligible performance degradation under continuous operation at ± 500 mA cm^{-2} for 1000 h (**Figure** 4a). In contrast, NFW displayed rapid performance deterioration, with marked decay observed within the first 500 h (Figure S27, Supporting Information). Furthermore, NFCW outperforms reported non-noble

metal electrocatalysts in HER and OER performance (Tables S9 and S10, Supporting Information). XRD results (Figure 4b; Figure S28, Supporting Information) show minimal shifts in peak position following both HER and OER, with noticeable variations in peak intensities. Prolonged HER increases crystallinity, while OER leads to a reduction in intensity, likely due to the accumulation of oxidative species. Aside from the peaks of the NiFeCo alloy, peaks observed at 11.6°, 23.4°, 34.7°, 38.4°, 59.8°, and 61.4° align with the characteristic peaks of NiFe LDH (PDF#40-0215), consistent with the SAED ring pattern in Figure S29 (Supporting Information).

To further probe structural evolution, transmission electron microscopy (TEM) analysis was conducted. As depicted in Figure 4c,d, NFCW retains its nanowire structural integrity even after prolonged HER and OER. Ni, Fe, and Co remain uniformly distributed along the nanowire core, while oxygen is predominantly localized within the surface oxide layer. Figure S30 (Supporting Information) demonstrates that, despite extended reduction reactions, residual oxidized species persist on the NFCW surface, indicative of oxidative reactions during system shutdown and confirming the influence of reverse current. Additionally, Figure S31 (Supporting Information) reveals trace amounts of Co deposited on the NFCW surface, originating from a dissolution-redeposition process. The Co-rich layer forms an impermeable barrier, effectively blocking electrolyte diffusion pathways and mitigating galvanic corrosion, thereby ensuring long-term operational stability under harsh electrochemical conditions. In contrast, NFW exhibits severe structural deterioration during HER (Figure 4f; Figure S32a, Supporting Information). The synergistic effects of periodic H_2 bubble stripping, cyclic volume expansion/contraction in alkaline media, and selective oxidative dissolution of Ni/Fe progressively fragment the nanowires into porous particle aggregates. Post-OER characterization (Figure 4g,h; Figure S32b, Supporting Information) reveals the formation of a thick, porous oxide layer on NFW, indicating active site depletion and structural collapse due to Ni/Fe dissolution. ICP-OES results (Tables S9 and S10, Supporting Information) show that the Ni/Fe ratio in NFCW remains stable after HER/OER, while the ratio in NFW increases after prolonged OER, indicating Fe leaching.

Fluctuations in electric current input during electrolysis can significantly compromise the durability of catalytic electrodes. To evaluate catalyst resilience under realistic operating conditions, accelerated durability tests were performed.[33] As shown in Figure 3i, NFCW maintains stable OER and HER performance after over 3000 potential cycles accelerated durability test (CV-ADT), demonstrating its resilience under complex and fluctuating conditions. XPS analysis (Figure S33, Supporting Information) indicates that NFCW retains a low-valence metal structure after the ADT test. The Ni and Fe peaks on the surface of NFCW shift toward lower valence states compared to NFW, indicating a smaller extent of structural changes. Based on ICP-OES results (Figure 4j; Tables S11 and S12, Supporting Information), after CV-ADT, the concentrations of Ni and Fe in the electrolyte of the NFW sample gradually increase, indicating continuous leaching of these elements. In contrast, the Ni and Fe concentrations in the Co-doped NFCW sample remain stable. These results suggest that Co doping significantly enhances the long-term stability of the NiFe catalyst by mitigating the leaching of active metal species, thereby maintaining structural integrity under repeated forward and reverse current cycling.

Generally, the decline in catalyst stability can be attributed to several factors, including the dissolution and reconstruction of active sites on the catalyst surface, dissolution of metal atoms, corrosion in highly alkaline environments, and bubble impact.[34] For Ni- and Fe-based catalysts, instability arises partially from the oxidation of Ni/Fe to higher valence states and their subsequent dissolution. This instability can be evaluated through the formation energies of Ni and Fe vacancies.[35] Figure 4k reveals that Ni and Fe vacancy formation energies are 1.42 and 1.79 eV for NFCW, respectively, compared to 0.82 and 1.23 eV in NFW. The higher vacancy formation energies of Ni and Fe in NFCW suppress the dissolution tendency, thereby enhancing the stability of the material. This is consistent with earlier findings,[36] where incorporating Co into the alloy adjusts the properties of the catalytic electrodes, thereby enhancing the stability of the catalyst structure and composition under fluctuating conditions.

2.4. AEMWE Performance and Optimization Mechanisms

The NFCW demonstrates exceptional bifunctionality, serving effectively as both anode and cathode in AEMWE. As illustrated in **Figure 5a**, the assembled AEMWE integrates key components, including end plates, Nickel-based current collectors, bipolar plates, gaskets, gas diffusion electrodes (GDEs), and an anion exchange membrane. In the symmetric NFCW || NFCW configuration, the device achieves high current densities of 1 A cm^{-1} at 1.81 V and 4 A cm^{-1} at 2.33 V without iR compensation (Figure 5b), benefiting from ultralow ohmic (R_{ohm}) and charge transfer resistances (R_{ct}). Performance improves linearly with rising electrolyte temperature (Figure S35, Supporting Information). The NFCW-based AEMWE achieves 935 mA cm^{-2}@2V in 0.1 M KOH and 520 mA cm^{-2}@2 V in pure water, with higher KOH concentrations reducing electrolyte and charge transfer resistances (Figure S36, Supporting Information). Compared to NFW and noble metal benchmarks, NFCW exhibits superior activity across a broad voltage range (Figure 5c).

To evaluate the tolerance of electrodes to fluctuating energy inputs, a critical requirement for coupling with renewable energy, the electrodes were subjected to rigorous dynamic ADT tests. While stable under constant current operation, electrodes show noticeable degradation under voltage and current square-wave cycling, revealing stability limitations under dynamic conditions. In order to simulate the sudden shut-down and start-up process, the electrodes were tested with potential square wave cycling between 0 and 2 V. The NFCW || NFCW configuration exhibits a slight decrease over 2000 cycles, whereas the NFW || NFW system shows significant performance loss (Figure 5d). This substantial difference is attributed to cobalt-mediated stabilization of the catalyst structure during rapid redox transitions. After 2000 cycles at 2 V, the NiFeCo alloy retains a substantially higher current density compared to the NiFe counterpart, which maintains only ≈40% of its initial value, highlighting the enhanced durability enabled by cobalt incorporation. Additionally, a current square wave test, alternating between 500 and −500 mA cm^{-2} over 1000 cycles, reveals stable voltage retention of NFCW, while NFW || NFW and IrO_2 || Pt/C experience notable voltage degradation (Figure 5e).

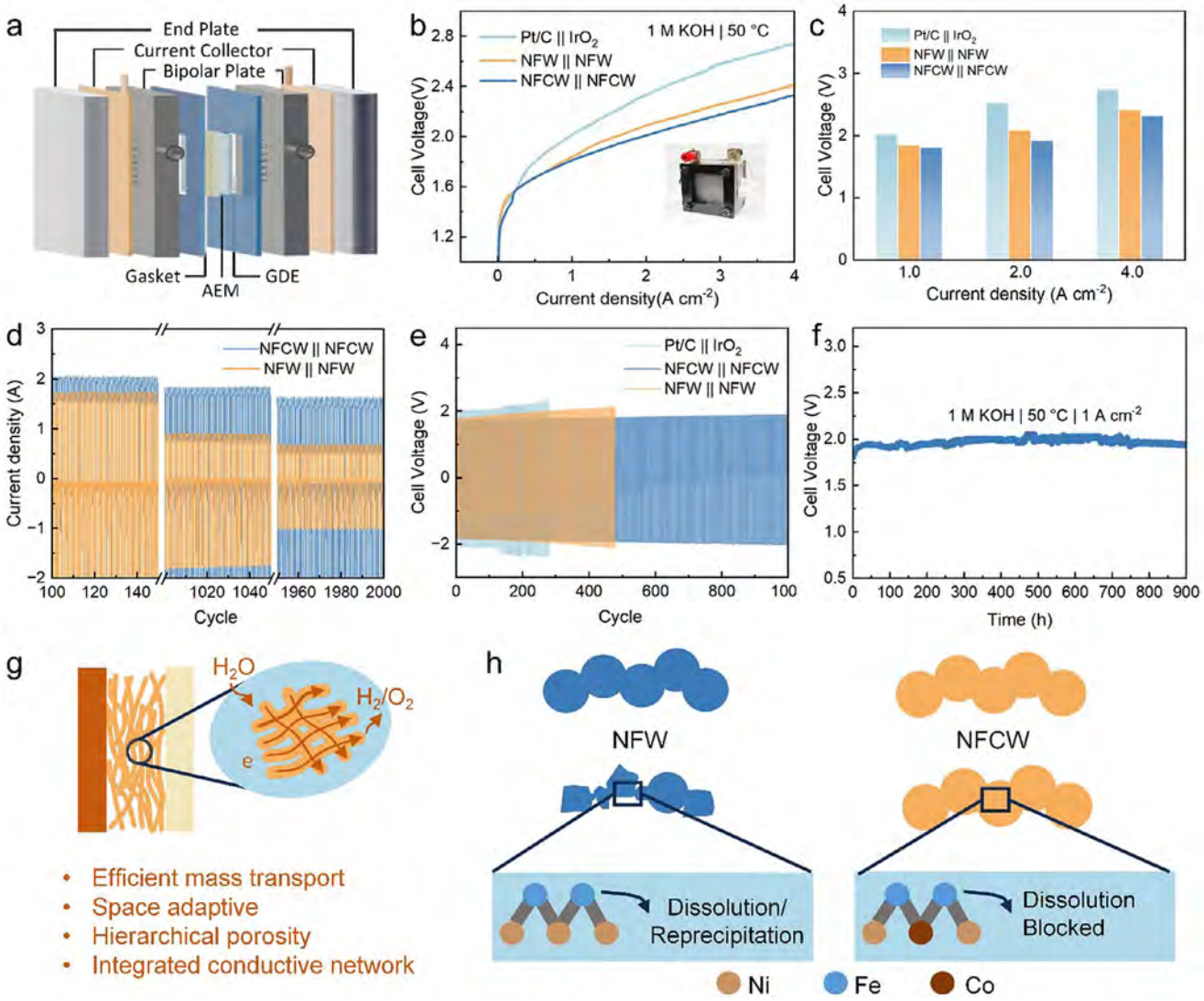

Figure 5. Electrolyzer performance and optimization mechanism. a) Schematic diagram of the AEMWE cell setup. b) Polarization curves of IrO_2 || Pt/C, NFW || NFW and NFCW || NFCW electrolyzer. c) Comparison of cell voltage at different current densities. d) Start-up and shut-down simulation square wave test between 2 (10 s) and 0 V (10 s). e) Reverse current cycling test between ± 500 mA cm^{-2}, each lasting 20 min. f) Stability of NFCW || NFCW at 1000 mA cm^{-2}. Curve fluctuations are due to electrolyte replacement. g) Illustration of the advantages of the integrated nanowire structure in enhancing activity and structural stability. h) Stability enhancement achieved through component regulation.

The NFCW-based AEMWE demonstrates excellent stability, with no significant voltage degradation observed over 900 h at 1000 mA cm^{-2} (Figure 5f).

This exceptional operational stability results from the synergistic effect of electronic and structural reinforcement. The integrated 1D nanowire architecture unifies catalytic activity and mass transport within a continuous conductive framework (Figure 5g). The ultrahigh specific surface area ensures abundant active site exposure, while the flexible nanowire framework accommodates mechanical stress during cell assembly and mitigates deformation from gas evolution. This hierarchical design enhances mass transport and structural resilience, ensuring reliable performance under dynamic operating conditions. Cobalt incorporation further strengthens electrochemical robustness by enhancing resistance to catalyst dissolution (Figure 5h). Strong electronic interactions between Co and Ni/Fe modulate the local charge density and elevate the energy barrier for vacancy formation, thereby suppressing active site leaching and prolonging catalyst lifespan. Collectively, these findings highlight NFCW as a highly promising electrode architecture for water electrolysis systems under intermittent and fluctuating power inputs, demonstrating both improved efficiency and enhanced durability suitable for renewable-energy-integrated applications.

3. Conclusion

This study addresses the long-standing challenge of reverse current-induced degradation in water electrolysis, which remains a major barrier to the stable and efficient integration of renewable energy into hydrogen production. We report a self-supported

ternary $Ni_{75}Fe_{15}Co_{10}$ nanowire electrode that combines high intrinsic activity with excellent mechanical resilience. Cobalt incorporation optimizes the electronic structure and promotes Ni–Fe–Co synergy, while increasing vacancy formation energy, leading to concurrent enhancements in activity and stability. The interconnected nanowire network facilitates efficient charge transport and stress dissipation, ensuring stable performance under intermittent and fluctuating power inputs. NFCW demonstrates outstanding electrocatalytic performance, enabling AEMWE operation at 4 A cm^{-2} with a low voltage of 2.33 V while maintaining stable activity under dynamic conditions. Unlike previous studies that primarily rely on steady-state performance metrics, this work systematically evaluates electrode performance under dynamic cycling after 2000 cycles of intermittent reverse current, the ternary electrode shows a ≈40% reduction in voltage decay rate compared to its binary NiFe counterpart, highlighting the stabilizing effect of cobalt. These results establish an important benchmark for robust alkaline water electrolysis and provide a viable strategy to mitigate reverse current-induced degradation, a long-standing challenge in coupling electrolysis systems with intermittent renewable energy sources.

Supporting Information

Supporting Information is available from the Wiley Online Library or from the author.

Acknowledgements

This research was supported by the National Natural Science Foundation of China (52273297, 12411530118), the Guangdong Provincial Key Laboratory of Thermal Management Engineering & Materials (2020B1212060015), the Guangdong Provincial Basic and Applied Basic Research Project (2024B1515120005), the Shenzhen Geim Graphene Center, Shenzhen Technical Project (JCYJ20241202123910015). The authors also thank the Testing Technology Center of Materials and Devices, Tsinghua Shenzhen International Graduate School, for instrumental support.

Conflict of Interest

The authors declare no conflict of interest.

Data Availability Statement

The data that support the findings of this study are available in the supplementary material of this article.

Keywords

hydrogen, nickel-based catalyst, renewable energy, reverse current, water electrolysis

Received: August 13, 2025
Revised: September 21, 2025
Published online: October 16, 2025

[1] J. A. Turner, *Science* **2004**, *305*, 972.
[2] Z.-Y. Yu, Y. Duan, X.-Y. Feng, X. Yu, M.-R. Gao, S.-H. Yu, *Adv. Mater.* **2021**, *33*, 2007100.
[3] M. Chatenet, B. G. Pollet, D. R. Dekel, F. Dionigi, J. Deseure, P. Millet, R. D. Braatz, M. Z. Bazant, M. Eikerling, I. Staffell, P. Balcombe, Y. Shao-Horn, H. Schäfer, *Chem. Soc. Rev.* **2022**, *51*, 4583.
[4] A. J. Shih, M. C. O. Monteiro, F. Dattila, D. Pavesi, M. Philips, A. H. M. da Silva, R. E. Vos, K. Ojha, S. Park, O. van der Heijden, G. Marcandalli, A. Goyal, M. Villalba, X. Chen, G. T. K. K. Gunasooriya, I. McCrum, R. Mom, N. López, M. T. M. Koper, *Nat Rev Methods Primers* **2022**, *2*, 84.
[5] M. A. Pellow, C. J. M. Emmott, C. J. Barnhart, S. M. Benson, *Energy Environ. Sci.* **2015**, *8*, 1938.
[6] T. M. Gür, *Energy Environ. Sci.* **2018**, *11*, 2696.
[7] Q. Sha, S. Wang, L. Yan, Y. Feng, Z. Zhang, S. Li, X. Guo, T. Li, H. Li, Z. Zhuang, D. Zhou, B. Liu, X. Sun, *Nature* **2025**, *639*, 360.
[8] A. Abdel Haleem, J. Huyan, K. Nagasawa, Y. Kuroda, Y. Nishiki, A. Kato, T. Nakai, T. Araki, S. Mitsushima, *J. Power Sources* **2022**, *535*, 231454.
[9] N. Guruprasad, J. van der Schaaf, M. T. de Groot, *J. Power Sources* **2024**, *613*, 234877.
[10] W. H. Lee, Y.-J. Ko, J. H. Kim, C. H. Choi, K. H. Chae, H. Kim, Y. J. Hwang, B. K. Min, P. Strasser, H.-S. Oh, *Nat. Commun.* **2021**, *12*, 4271.
[11] S.-M. Jung, Y. Kim, B.-J. Lee, H. Jung, J. Kwon, J. Lee, K.-S. Kim, Y.-W. Kim, K.-J. Kim, H.-S. Cho, J. H. Park, J. W. Han, Y.-T. Kim, *Adv. Funct. Mater.* **2024**, *34*, 2316150.
[12] R. A. Krivina, G. A. Lindquist, S. R. Beaudoin, T. N. Stovall, W. L. Thompson, L. P. Twight, D. Marsh, J. Grzyb, K. Fabrizio, J. E. Hutchison, S. W. Boettcher, *Adv. Mater.* **2022**, *34*, 2203033.
[13] C. Feng, F. Wang, Z. Liu, M. Nakabayashi, Y. Xiao, Q. Zeng, J. Fu, Q. Wu, C. Cui, Y. Han, N. Shibata, K. Domen, I. D. Sharp, Y. Li, *Nat. Commun.* **2021**, *12*, 5980.
[14] F.-Y. Chen, Z.-Y. Wu, Z. Adler, H. Wang, *Joule* **2021**, *5*, 1704.
[15] G. Wang, H. Li, F. Babbe, A. Tricker, E. J. Crumlin, J. Yano, R. Mukundan, X. Peng, *Adv. Energy Mater.* **2025**, *15*, 2500886.
[16] S. Holmin, L.-Å. Näslund, Á. S. Ingason, J. Rosen, E. Zimmerman, *Electrochim. Acta* **2014**, *146*, 30.
[17] C. Kuai, Z. Xu, C. Xi, A. Hu, Z. Yang, Y. Zhang, C.-J. Sun, L. Li, D. Sokaras, C. Dong, S.-Z. Qiao, X.-W. Du, F. Lin, *Nat. Catal.* **2020**, *3*, 743.
[18] D. Y. Chung, P. P. Lopes, P. Farinazzo Bergamo Dias Martins, H. He, T. Kawaguchi, P. Zapol, H. You, D. Tripkovic, D. Strmcnik, Y. Zhu, S. Seifert, S. Lee, V. R. Stamenkovic, N. M. Markovic, *Nat. Energy* **2020**, *5*, 222.
[19] B. M. Hunter, N. B. Thompson, A. M. Müller, G. R. Rossman, M. G. Hill, J. R. Winkler, H. B. Gray, *Joule* **2018**, *2*, 747.
[20] V. Okatenko, A. Loiudice, M. A. Newton, D. C. Stoian, A. Blokhina, A. N. Chen, K. Rossi, R. Buonsanti, *J. Am. Chem. Soc.* **2023**, *145*, 5370.
[21] J. Hao, Z. Zhuang, K. Cao, G. Gao, C. Wang, F. Lai, S. Lu, P. Ma, W. Dong, T. Liu, M. Du, H. Zhu, *Nat. Commun.* **2022**, *13*, 2662.
[22] X. Yang, J. Liang, Q. Shi, M. J. Zachman, S. Kabir, J. Liang, J. Zhu, B. Slenker, M. Pupucevski, N. Macauley, A. J. Kropf, H. Zeng, D. Strasser, D. J. Myers, H. Xu, Z. Zeng, Y. Yan, G. Wu, *Adv. Energy Mater.* **2024**, *14*, 2400029.
[23] H. Ali-Löytty, M. W. Louie, M. R. Singh, L. Li, H. G. Sanchez Casalongue, H. Ogasawara, E. J. Crumlin, Z. Liu, A. T. Bell, A. Nilsson, D. Friebel, *J. Phys. Chem. C* **2016**, *120*, 2247.
[24] C. Liang, P. Zou, A. Nairan, Y. Zhang, J. Liu, K. Liu, S. Hu, F. Kang, H. J. Fan, C. Yang, *Energy Environ. Sci.* **2020**, *13*, 86.
[25] L. Magnier, G. Cossard, V. Martin, C. Pascal, V. Roche, E. Sibert, I. Shchedrina, R. Bousquet, V. Parry, M. Chatenet, *Nat. Mater.* **2024**, *23*, 252.

[26] M. C. Biesinger, B. P. Payne, A. P. Grosvenor, L. W. M. Lau, A. R. Gerson, R. St C Smart, *Appl. Surf. Sci.* **2011**, *257*, 2717.
[27] X. Duan, F. Cao, R. Ding, X. Li, Q. Li, R. Aisha, S. Zhang, K. Hua, Z. Rui, Y. Wu, J. Li, A. Li, J. Liu, *Adv. Energy Mater.* **2022**, *12*, 2103144.
[28] C. Feng, X. She, Y. Xiao, Y. Li, *Angew. Chem., Int. Ed.* **2023**, *62*, 202218738.
[29] F. Bao, E. Kemppainen, I. Dorbandt, F. Xi, R. Bors, N. Maticiuc, R. Wenisch, R. Bagacki, C. Schary, U. Michalczik, P. Bogdanoff, I. Lauermann, R. van de Krol, R. Schlatmann, S. Calnan, *ACS Catal.* **2021**, *11*, 10537.
[30] B. S. Yeo, A. T. Bell, *J. Phys. Chem. C* **2012**, *116*, 8394.
[31] B. K. Kim, M. J. Kim, J. J. Kim, *Appl. Catal., B* **2022**, *308*, 121226.
[32] L. Lu, C. Wen, H. Wang, Y. Li, J. Wu, C. Wang, *J. Catal.* **2023**, *424*, 1.
[33] R. A. Marquez, M. Espinosa, E. Kalokowski, Y. J. Son, K. Kawashima, T. V. Le, C. E. Chukwuneke, C. B. Mullins, *ACS Energy Lett.* **2024**, *9*, 547.
[34] C. Spöri, J. T. H. Kwan, A. Bonakdarpour, D. P. Wilkinson, P. Strasser, *Angew. Chem., Int. Ed.* **2017**, *56*, 5994.
[35] Y. Hu, M. Zhu, X. Luo, G. Wu, T. Chao, Y. Qu, F. Zhou, R. Sun, X. Han, H. Li, B. Jiang, Y. Wu, X. Hong, *Angew. Chem., Int. Ed.* **2021**, *60*, 6533.
[36] Y. Yang, S. Wei, Y. Li, D. Guo, H. Liu, L. Liu, *Appl. Catal., B* **2022**, *314*, 121491.